Dalton
Transactions

PAPER

View Article Online
View Journal | View Issue

Check for updates

Cite this: *Dalton Trans.*, 2024, **53**, 12943

Dual-nodes bridged cobalt-modified Keggin-type polyoxometalate-based chains for highly efficient CO_2 photoconversion†

Xin-Lian Chen, Jie Wu, Ji-Lei Wang, Xiao-Mei Liu, Hua Mei* and Yan Xu *

The design of efficient catalysts for photocatalytic CO_2 conversion is of great importance for the sustainable development of society. Herein, three polyoxometalate (POM)-based crystalline materials were formulated prepared by substituting transition metals and adjusting solvent acidity with 2-(2-pyridyl) benzimidazole (pyim) as the light-trapping ligand, namely $\{[SiW_{12}O_{40}][Co(pyim)_2]_2\}\cdot 2C_2H_5OH$ (**$SiW_{12}Co_2$**), $\{[SiW_{12}O_{40}][Ni(pyim)_2]_2\}\cdot 2C_2H_5OH$ (**$SiW_{12}Ni_2$**), and $\{[SiW_{12}O_{40}][Mn(pyim)_2]_2\}\cdot 2C_2H_5OH$ (**$SiW_{12}Mn_2$**). X-ray crystallography diffraction analysis indicates that the three complexes exhibit isostructural properties, and form a stable one-dimensional chain structure stabilized by two $[M(pyim)_2]_2^{2+}$ (M = Co, Ni, and Mn) fragments serving as dual-nodes to the adjacent SiW_{12} units. A comprehensive analysis of the structural characterization and photocatalytic CO_2 reduction properties is presented. Under light irradiation, **$SiW_{12}Co_2$** exhibited a remarkable CO generation rate of 10 733 μmol g^{-1} h^{-1} with a turnover number of 328, outperforming most of the reported heterogeneous POM-based photocatalysts. Besides, cycling tests revealed that **$SiW_{12}Co_2$** is an efficient and stable photocatalyst with great recyclability for at least four successive runs. This study proves that the successful incorporation of diverse transition metals into the POM anion could facilitate the development of highly efficient photocatalysts for the CO_2RR.

Received 17th June 2024,
Accepted 11th July 2024

DOI: 10.1039/d4dt01757a

rsc.li/dalton

Introduction

The continued massive consumption of non-renewable fossil fuels and increasing level of industrialization have reached a significant level of unsustainable development in recent years, and a serious energy crisis has been triggered.[1–4] Moreover, the large amount of CO_2 emissions has led to global climate change, such as the greenhouse effect.[5–8] One of the most effective strategies to mitigate the greenhouse effect and bring about the carbon cycle is converting CO_2 into valuable products (CO, CH_4, *etc.*).[9–15] Until now, the conversion of solar energy into chemical energy through photocatalytic reactions has been widely studied in numerous fields. Compared with traditional catalytic methods, the most promising approach for efficient and sustainable energy production and conversion is to transform atmospheric carbon dioxide into renewable energy substitutes.[16–19] Currently, the solar-driven catalytic reduction of carbon dioxide to hydrocarbon fuels (*e.g.*, CO, CH_4, C_2H_4, C_2H_6) or chemicals (*e.g.*, HCOOH, CH_3OH, CH_3COOH) is a crucial and environmentally friendly but challenging approach for carbon recovery.[20–23] Hence, it is necessary to develop efficient and selective catalysts.

It is a truth universally acknowledged that polyoxometalates (POMs) possess exceptional redox capacity and well-defined structures. Also, the structural dimensions can be adjusted by changing the constituent elements and organic bridging components.[24–30] Furthermore, multiple electrons and protons can be stored while also allowing for rapid photo-responsive charge transfer and reversible redox reactions. Along with providing rich redox electron pairs, transition metals (such as Co, Ni, Mn, *etc.*) serve as sites of catalysis. Furthermore, they can unite with lacunary POMs to generate an array of polyoxometalates replaced with transition metals. Thus, researchers are increasingly interested in POM-based inorganic–organic hybrid materials that combine POMs with metal ions and organic ligands, given that POMs contain a large number of oxygen atoms on their outer surface, which can coordinate with metal ions or organic units to generate novel compounds.[31–37] Yao and co-workers synthesized the first POM in 2019 comprising a nuclear Co cluster that had effective photocatalytic activity for CO_2 reduction. The maximum values of TON and TOF exhibited were 10 492 and 0.29 s^{-1}, respectively.[38] In 2020, Zhang's group reported a significant tungsten-substituted TiO_2, which contributed to the

---

College of Chemical Engineering, State Key Laboratory of Materials-Oriented Chemical Engineering, Nanjing Tech University, Nanjing 211800, P. R. China. E-mail: yanxu@njtech.edu.cn

† Electronic supplementary information (ESI) available: Synthesis, details of crystallographic data, structural figures, PXRD patterns, and IR spectra characterization. CCDC 2359927–2359929. For ESI and crystallographic data in CIF or other electronic format see DOI: https://doi.org/10.1039/d4dt01757a

generation of Ti vacancies that served as catalytically active sites for reducing CO_2.[39] Based on the above considerations, the objective was to enhance photocatalysis by incorporating Co, Ni, and Mn elements separately into tungsten-containing POMs to generate novel compounds.

In view of the aforementioned literature, we utilized 2-(2-pyridyl)benzimidazole (pyim) as an organic ligand, and $\{SiW_{12}O_{40}\}$ as the molecular unit to construct new compounds with transition metal ions (Co, Ni, and Mn) to use as linkers in order to generate three novel Keggin-type $\{SiW_{12}O_{40}\}$-based 1D chains under hydrothermal conditions: $\{[SiW_{12}O_{40}][Co(pyim)_2]_2\}\cdot 2C_2H_5OH$ (**$SiW_{12}Co_2$**), $\{[SiW_{12}O_{40}][Ni(pyim)_2]_2\}\cdot 2C_2H_5OH$ (**$SiW_{12}Ni_2$**), and $\{[SiW_{12}O_{40}][Mn(pyim)_2]_2\}\cdot 2C_2H_5OH$ (**$SiW_{12}Mn_2$**). All three compounds are composed of $\{SiW_{12}O_{40}\}$ units, transition metals, and ligands in a three-dimensional supramolecular structure. Notably, **$SiW_{12}Co_2$** exhibits the highest catalytic activity in the photocatalytic CO_2RR. When 0.54 μmol of **$SiW_{12}Co_2$** was introduced, the turnover numbers (TON) of CO and H_2 achieved the values of 328 and 181, respectively, where the yields were, respectively, 177.1 and 97.6 μmol, and the production rates were 10 733 and 6100 μmol g^{-1} h^{-1} under eight-hour irradiation periods. **$SiW_{12}Ni_2$** has only weak photocatalytic CO_2RR activity, but it does provide a higher CO/H_2 ratio and optimum selectivity for CO (82.5%). Additionally, **$SiW_{12}Co_2$** possesses excellent chemical stability, enabling it to maintain its structural integrity after four catalytic cycles.

Experimental section

Synthesis of compounds

$\{[SiW_{12}O_{40}][Co(pyim)_2]_2\}\cdot 2C_2H_5OH$ ($SiW_{12}Co_2$). A solution was prepared by dissolving the mixture of $H_4[SiW_{12}O_{40}]\cdot 6H_2O$ (0.4480 g, 0.15 mmol), $Co(OAc)\cdot 4H_2O$ (0.1245 g, 0.50 mmol), and pyim (0.0400 g, 0.20 mmol) in 12 mL of mixed solvent [(water) : (ethanol) = 8 : 4 v/v] and stirring for 0.5 h at room temperature. Then, NaOH (1 M) was used to modulate the pH to approximately 3.0, and the resulting mixture was stirred for a further half hour. Subsequently, the aforementioned mixture was sealed within a Teflon-lined stainless-steel autoclave and maintained at 170 °C for a period of 3 days. Ultimately, once room temperature was reached, orange-red parallelogram block crystals were extracted using filtration and cleaned with distilled water. Yield: 45% (based on pyim). Found (%): C, 15.56; H, 1.12; N, 4.66; anal. calcd (%): C, 15.71; H, 1.10; N, 4.40. IR (KBr pellet, cm^{-1}): 3444 (m), 2931 (w), 1600 (m), 1439 (m), 1383 (s), 1012 (m), 924 (s), 796 (s) (Fig. S10a†).

$\{[SiW_{12}O_{40}][Ni(pyim)_2]_2\}\cdot 2C_2H_5OH$ ($SiW_{12}Ni_2$). The synthetic procedure of **$SiW_{12}Ni_2$** is analogous to that of **$SiW_{12}Co_2$**, except that $Co(OAc)_2\cdot 4H_2O$ (0.1245 g, 0.50 mmol) was substituted for $Ni(OAc)_2\cdot 4H_2O$ (0.1244 g, 0.50 mmol). The solution pH was adjusted to about 3.0 with HCl (1 M). **$SiW_{12}Ni_2$** exhibited yellow-green parallelogram block crystals. Yield: 42% (based on pyim). Found (%): C, 15.47; H, 1.07; N, 4.64; anal. calcd (%): C, 15.71; H, 1.10; N, 4.40. IR (KBr pellet, cm^{-1}): 3386 (m), 2918 (w), 1604 (m), 1442 (m), 1384 (s), 1012 (m), 924 (s), 799 (s) (Fig. S10b†).

$\{[SiW_{12}O_{40}][Mn(pyim)_2]_2\}\cdot 2C_2H_5OH$ ($SiW_{12}Mn_2$). The synthetic procedure of **$SiW_{12}Mn_2$** is analogous to that of $SiW_{12}Co_2$, except that $Co(OAc)_2\cdot 4H_2O$ (0.1245 g, 0.50 mmol) was replaced with $Mn(OAc)_2\cdot 4H_2O$ (0.1225 g, 0.50 mmol). HCl (1 M) was added to the solution to adjust its pH to 3.5. Orange parallelogram block crystals were eventually produced. Yield: 34% (based on pyim). Found (%): C, 15.50; H, 1.07; N, 4.70; anal. calcd (%): C, 15.74; H, 1.10; N, 4.44. IR (KBr pellet, cm^{-1}): 3378 (m), 2925 (w), 1601 (m), 1439 (m), 1442 (s), 1016 (m), 923 (s), 806 (s) (Fig. S10c†).

Results and discussion

Crystal structure

X-ray diffraction crystallography analysis indicated that these three compounds exhibit semblable primary structures where only the transition metals present differences, and that they all crystallize in the triclinic system with a $P\bar{1}$ space group (Table 1). The surface morphology of the crystals of **$SiW_{12}M_2$** (M = Co, Ni, and Mn) has been clearly visualized under an optical microscope (Fig. S1†) and mapped by scanning electron microscopy (Fig. S14–S16†). Since the three compounds are isostructural, only **$SiW_{12}Co_2$** is exemplified here for a better understanding of its structure. There are basically two components that comprise the compounds: $[SiW_{12}O_{40}]^{4-}$ and $[Co(pyim)_2]^{2+}$ (Fig. 1a and b). The asymmetric unit of the compounds comprises half of one $\{SiW_{12}O_{40}\}$ node, two transition metal ions, four pyim ligands, as well as two free ethanol molecules (Fig. S2 and S6†). There is only one kind of metal-coordinated environment in the Co cluster. Each Co atom is connected to two pyim ligands (Fig. 1a). In concrete terms, two Co ions are both in a hexacoordinated environment, with 4 N atoms from 2 pyim ligands and 2 O atoms from two adjacent $\{SiW_{12}O_{40}\}$ units, with the unit exhibiting a common distorted octahedral geometry (Fig. S3 and S6b†). Also, there exists only one type of coordination environment for pyim in the structure. The ball-shaped cluster $\{SiW_{12}O_{40}\}$ is widely perceived as a heteroatomic α-Keggin POM with twelve tungsten atoms surrounding the central silicon atom with an approximate size of 10.4 Å × 10.4 Å (Fig. 1b). Twelve tungsten ions are distributed in three layers from top to bottom in a "3 + 6 + 3" arrangement. The $\{SiW_{12}O_{40}\}$ node can be viewed as a four-connected linkage to coordinate four Co ions by W–O–Co bonds (Fig. S6a†). Two adjacent POM units are connected to each other by two transition metal complex units, generating an infinite 1D chain-like structure (Fig. 1c). Moreover, Fig. 1d shows the simplified structure of a one-dimensional chain, in which purple balls represent the $[Co(pyim)_2]_2^{2+}$ fragments while yellow balls denote the Keggin POM. Two adjacent POMs in 1D chains form dual-nodes through two $[Co(pyim)_2]_2^{2+}$ fragments. Compared with most polyoxometalate compounds, a common prominent structural feature of these three compounds is the dual nodes of transition metals, which make their structures more stable than typical structures.[40,41,58]

Table 1 Crystallographic information for the three compounds

Complexes	$\mathbf{SiW_{12}Co_2}$	$\mathbf{SiW_{12}Ni_2}$	$\mathbf{SiW_{12}Mn_2}$
Formula	$C_{52}H_{48}N_{12}Co_2O_{42}SiW_{12}$	$C_{52}H_{48}N_{12}Ni_2O_{42}SiW_{12}$	$C_{52}H_{48}N_{12}Mn_2O_{42}SiW_{12}$
Formula weight	3865.17	3864.73	3857.19
T (K)	293(2)	293(2)	293(2)
Crystal system	Triclinic	Triclinic	Triclinic
Space group	$P\bar{1}$	$P\bar{1}$	$P\bar{1}$
a (Å)	11.981(9)	11.9589(16)	11.974(8)
b (Å)	12.240(9)	12.1998(16)	12.380(8)
c (Å)	14.091(11)	14.0482(19)	14.074(9)
α (°)	101.102(9)	101.336(2)	101.321(8)
β (°)	98.930(10)	98.179(2)	98.243(8)
γ (°)	108.668(9)	108.916(2)	108.981(7)
V (Å^3)	1868(2)	1853.6(4)	1886(2)
Z	1	1	1
D_c (mg m^{-3})	3.436	3.462	3.397
μ (mm^{-1})	18.937	19.145	18.656
F (000)	1736	1738	1732
θ range (°)	1.515–25.010	1.516–25.006	1.514–25.009
Crystal size (mm^3)	0.13 × 0.12 × 0.11	0.13 × 0.12 × 0.11	0.13 × 0.12 × 0.11
Limiting indices	$-13 \le h \le 14$, $-14 \le k \le 14$, $-16 \le l \le 16$	$-14 \le h \le 14$, $-14 \le k \le 13$, $-16 \le l \le 16$	$-14 \le h \le 14$, $-14 \le k \le 14$, $-16 \le l \le 14$
Reflections collected	13 284	13 205	13 205
R(int)	0.0877	0.0670	0.0591
Data/restraints/parameters	6532/207/567	6455/233/567	6578/222/567
GOF	1.202	1.171	1.181
$R_1{}^a$, w$R_2{}^b$[$I > 2\sigma(I)$]	$R_1 = 0.0729$, w$R_2 = 0.1748$	$R_1 = 0.0687$, w$R_2 = 0.1956$	$R_1 = 0.0648$, w$R_2 = 0.1541$
R_1, wR_2 (all data)	$R_1 = 0.0827$, w$R_2 = 0.1788$	$R_1 = 0.0778$, w$R_2 = 0.1998$	$R_1 = 0.0687$, w$R_2 = 0.1559$

[a] $R_1 = \sum||F_o| - |F_c||/\sum|F_o|$. [b] $wR_2 = \sum[w(F_o{}^2 - F_c{}^2)^2]/\sum[w(F_o{}^2)^2]^{1/2}$.

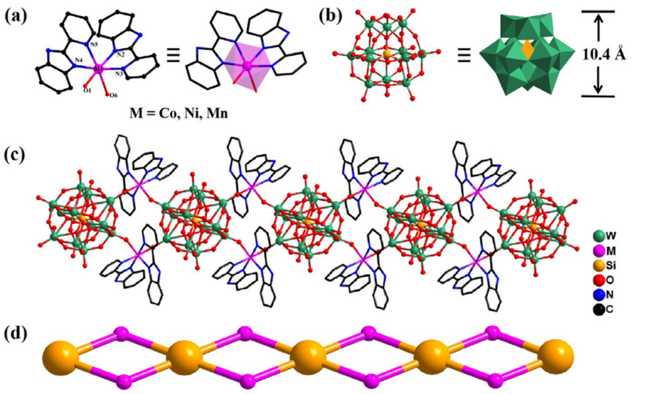

Fig. 1 The structure of $\mathbf{SiW_{12}M_2}$ (M = Co, Ni, Mn): (a) the coordinating surroundings of the M node; (b) structure of the {$SiW_{12}O_{40}$} node; (c and d) 1D chain composed of M and {$SiW_{12}O_{40}$} and the simplified structure of the 1D chain.

In addition, adjacent 1D chains are arranged regularly to shape 2D supramolecular layers through π–π stacking interactions between pyim ligands, while the distance between layers is 9.2 Å (Fig. 2a, and S7†), and adjacent 2D supramolecular layers further contribute to the formation of the 3D supramolecular structure shown in Fig. 2b, facilitated by weak π–π stacking interactions between them. Based on bond valence sum (BVS) calculations, the valence states of M^{II} in these compounds were ascertained. The Co–O/N bonds range between 2.065(7) and 2.193(15) Å, all within the normal range of M^{II} compounds reported in the literature.[42]

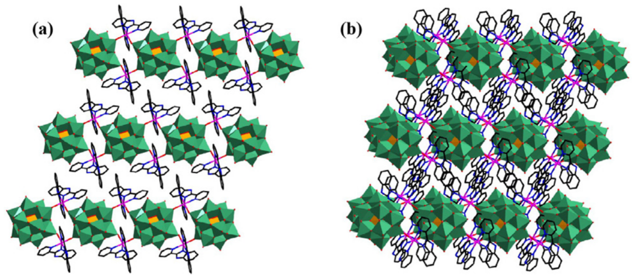

Fig. 2 (a) The 2D stacking diagram of $\mathbf{SiW_{12}Co_2}$; (b) the 3D supramolecular framework of $\mathbf{SiW_{12}Co_2}$.

Characterization

The PXRD patterns of these three compounds were first recorded at room temperature. The experimental results of the three samples can be well matched with the simulated patterns, proving the high phase purity of samples. Additionally, these compounds exhibit comparable diffraction peaks (Fig. S9†), demonstrating that they are isomorphic compounds. The conclusion is compatible with the results obtained from the resolution of the single-crystal structure. Subsequently, infrared (IR) spectra were produced to confirm the coordinated environment. As depicted in Fig. S10,† the IR spectra of these three isostructural compounds are analogous. Thus, analyzing the spectrum only for $\mathbf{SiW_{12}Co_2}$ as an example, the broad peak at 3444 cm^{-1} is assigned to the O–H stretching vibration; the peaks near 1012 and 924 cm^{-1} are identified as being the characteristic signals of Si–O and

W═O, respectively, while the W–O–W vibration of the polyacid SiW_{12} unit is observed at around 796 cm^{-1}. Furthermore, the peak at 2931 cm^{-1} indicates the antisymmetric and symmetric stretching vibration of C–H, while the peaks in the range of 1600–1383 cm^{-1} are stretching vibration signals for C═N, C═C, and C–N (Fig. S9a†). The results reveal successful ligand insertion with a coordination bond.

As effective absorption of sunlight is a prerequisite to photocatalysis, the light absorption range of these catalysts was characterized with UV-vis absorption spectroscopy. Taking **$SiW_{12}Co_2$** as an example, the SiW_{12} unit only absorbs in the UV range, whereas $Co(OAc)_2$ absorbs in the visible region (Fig. S11†), demonstrating that the absorption range of **$SiW_{12}Co_2$** can be expanded by doping transition metals into the POMs up to a maximum absorption edge of 700 nm (Fig. 3a). The band gap energy of **$SiW_{12}Co_2$** was further determined to be 2.55 eV *via* the Tauc plot (Fig. 3b), indicating that it has semiconductor-like characteristics. The energy is lower than that of the SiW_{12} unit, which is 3.15 eV (Fig. S12c†), implying that it has both structural stability and potentially photocatalytic capability in CO_2RR catalytic systems.

Furthermore, to precisely ascertain electronic band locations, Mott–Schottky (MS) plot measurements were conducted at different frequencies: 2000 Hz, 2500 Hz, and 3000 Hz. The LUMO energy value was found to be −0.85 V (Fig. 3c). This sufficiently negative LUMO level demonstrated that the compound was able to turn CO_2 into CO, CH_4, *etc.* According to the results of the bandgap and MS plot, the band structure diagram of **$SiW_{12}Co_2$** was obtained (Fig. 3d). In comparison with the normal hydrogen electrode (NHE), the conduction band (CB) position of **$SiW_{12}Co_2$** is −0.85 V, which is below the reduction potential required for CO generation (CO_2/CO = −0.53 V *vs.* NHE), which indicates that **$SiW_{12}Co_2$** would be able to catalyze the CO_2 photosynthetic reaction in theory.[43–47]

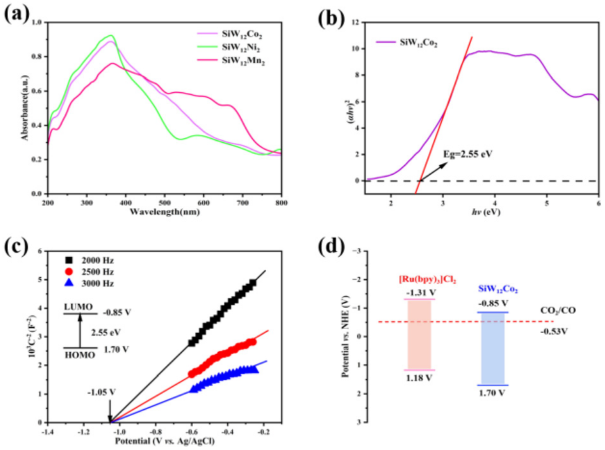

Fig. 3 (a) The UV-vis spectra of the three compounds; (b) band gap energy (E_g) analysis of **$SiW_{12}Co_2$**; (c) Mott–Schottky plots for **$SiW_{12}Co_2$**; (d) band-structure diagrams of **$SiW_{12}Co_2$**.

Photocatalytic CO_2 reduction

In accordance with the aforementioned UV-vis, Mott–Schottky, and energy band analysis, we utilized these **$SiW_{12}M_2$** crystalline materials as photocatalysts for photocatalytic CO_2 reduction reactions (CO_2RR) in a CH_3CN solvent system containing the sacrificial reagent triethanolamine (TEOA) and photosensitizer $[Ru(bpy)_3]Cl_2·6H_2O$ under a pure atmosphere of CO_2 (1.0 atm, 6 °C). All CO_2RRs were conducted in a thorough inquiry of the gas–liquid–solid system under visible light conditions (λ = 420–800 nm). First, the three catalysts were used as photocatalysts, respectively, where the production of H_2, CO, and CH_4 was detected, although the trace yield of methane is not reflected in the figures. As illustrated in Fig. 4a, we employed the identical molar amount (2.7 μmol) of catalyst and observed that the photocatalytic activity of **$SiW_{12}Co_2$** exhibited a notably greater performance than **$SiW_{12}Ni_2$** and **$SiW_{12}Mn_2$** in the CO_2RR. The main products of the reaction were CO (278.1 μmol) and H_2 (222.2 μmol). The growth trend of CO increased linearly in an approximate time-dependent manner, demonstrating the relative stability of the photoreduction process within the initial 8 h (Fig. 4d). On comparing with **$SiW_{12}Co_2$**, **$SiW_{12}Ni_2$** presents only weak photocatalytic CO_2RR activity, but it does provide a superior CO/H_2 ratio and optimum selectivity for CO (82.5%), which can be

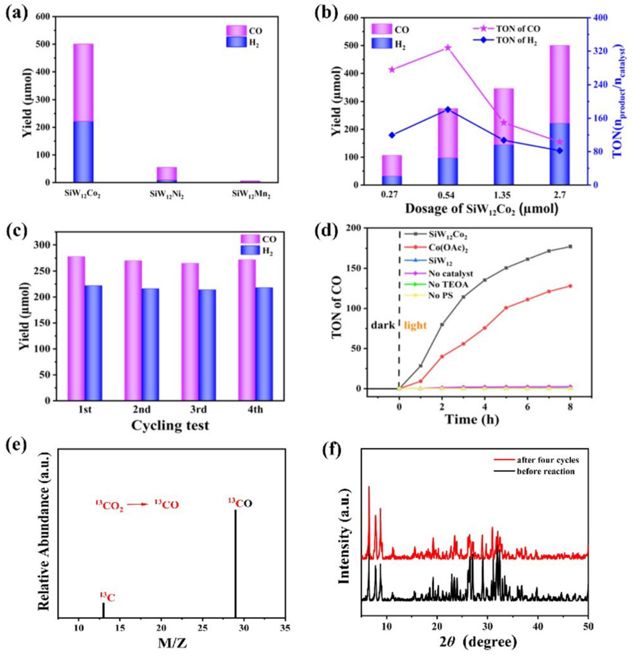

Fig. 4 (a) Comparison of the CO and H_2 yields in the photocatalytic system with **$SiW_{12}M_2$** as catalysts. (b) The impact of various **$SiW_{12}Co_2$** amounts on the yields of CO and H_2 (left axis) and the TON (right axis). (c) The change of CO and H_2 production when **$SiW_{12}Co_2$** was used as catalyst after each cycle. (d) Comparison of the TON values under different photocatalysts. (e) The mass spectrum of ^{13}CO (m/z = 29) generated by **$SiW_{12}Co_2$**. (f) The XRD patterns of **$SiW_{12}Co_2$** before the reaction and after four reaction cycles. Reaction conditions: $[Ru(bpy)_3]Cl_2·6H_2O$ (0.015 mmol), mixed solvents (50 mL, MeCN/TEOA, 4/1 v/v).

related to the higher capability of the Ni site to bind with high affinity. With regard to $\mathbf{SiW_{12}Mn_2}$, only trace amounts of CO and H_2 are produced under identical reaction conditions.

In consideration of the higher catalytic activity of $\mathbf{SiW_{12}Co_2}$, the effect of $\mathbf{SiW_{12}Co_2}$ dosage on the CO_2RR was further assessed. As clarified in Fig. 4b, the amounts of CO and H_2 are raised as the quantity of $\mathbf{SiW_{12}Co_2}$ is increased. With the addition of more catalyst (1.35, 2.7 μmol), the TON values of CO and H_2 were dramatically reduced. When 0.54 μmol of $\mathbf{SiW_{12}Co_2}$ was introduced, the turnover numbers (TON) of CO and H_2 achieved their highest values of 328 and 181, respectively, which are higher than those reported for most nonhomogeneous POM-based photocatalysts (Table S4†). Additionally, the yields were 177.1 and 97.6 μmol along with product rates that were 10 733 and 6100 μmol g^{-1} h^{-1} under eight-hour visible-light irradiation, respectively.

In addition, a succession of deletional comparative experiments with $\mathbf{SiW_{12}Co_2}$ were carried out to assess the different influence of each component of the photocatalytic reaction conditions. The results are displayed in Fig. 4d and Table 2. A control experiment in the absence of $\mathbf{SiW_{12}Co_2}$ showed that only trace amounts of products were generated, indicating that $\mathbf{SiW_{12}Co_2}$ is indeed significantly important for the photocatalytic reaction (entry 4). Nothing was detected under dark reaction conditions, indicating that the reaction was a light-driven catalytic reaction (entry 5). Moreover, in the absence of $[Ru(bpy)_3]Cl_2{\cdot}6H_2O$ or TEOA, gaseous or liquid products were hardly detected, suggesting that photosensitizers and sacrificial agents were critical for these photocatalysts in facilitating overall CO_2 reduction (entries 6 and 7). When exchanging CO_2 for Ar, only H_2 was detected, with no detectable levels of CO or CH_4, manifesting that CO_2 was the sole contributor of carbon (entry 8). Noteworthily, when separately using equimolar amounts of the SiW_{12} unit and $Co(OAc)_2$ instead of $\mathbf{SiW_{12}Co_2}$ under the same reaction conditions, the SiW_{12} showed hardly any catalytic activity, whereas $Co(OAc)_2$ exhibited average catalytic levels (CO, 128.0 μmol, H_2, 58.1 μmol), manifesting that the Co ion in $\mathbf{SiW_{12}Co_2}$ would be the main active center in CO_2 photoreduction (entries 2 and 3). In an effort to ensure the contribution of carbon over resultant gases, isotope studies were also conducted using $^{13}CO_2$ as a substrate under photocatalytic reaction conditions. The peak m/z = 29, as seen in Fig. 4e, is identified as ^{13}CO, revealing that $\mathbf{SiW_{12}Co_2}$ is in fact able to effectively reduce CO_2. The results of the above comparative experiments demonstrate that $[Ru(bpy)_3]Cl_2{\cdot}6H_2O$, TEOA, and $\mathbf{SiW_{12}Co_2}$ are indispensable in the photocatalytic CO_2 reduction system.

Table 2 Comparison of the yield of product under different photocatalysts and reaction conditions

Entry	Catalysts	Dosage (μmol)	CO (μmol)	H_2 (μmol)	CH_4 (μmol)	Notes
1[a]	$\mathbf{SiW_{12}Co_2}$	0.54	177.1	97.6	1.31	Hetero.
2[b]	SiW_{12}	0.54	0.59	21.2	0.34	Homo.
3[c]	Co $(OAc)_2$	1.08	128.0	58.1	1.61	Homo.
4[d]	No catalysts	—	2.52	3.63	0.68	Homo.
5[e]	$\mathbf{SiW_{12}Co_2}$	0.54	—	—	—	Hetero.
6[f]	$\mathbf{SiW_{12}Co_2}$	0.54	0.04	—	0.31	Hetero.
7[g]	$\mathbf{SiW_{12}Co_2}$	0.54	0.14	—	0.48	Hetero.
8[h]	$\mathbf{SiW_{12}Co_2}$	0.54	—	102.0	—	Hetero.

[a] Reaction conditions: $\mathbf{SiW_{12}Co_2}$ (0.54 μmol), $[Ru(bpy)_3]Cl_2{\cdot}6H_2O$ (0.015 mmol), mixed solvents (50 mL, MeCN/TEOA, 4/1 v/v), CO_2 (1 atm), λ = 420–800 nm, 6 °C, 8 h, 5.2 × 105 cd. [b] SiW_{12} replaced $\mathbf{SiW_{12}Co_2}$. [c] $Co(OAc)_2$ instead of $\mathbf{SiW_{12}Co_2}$. [d] No catalyst. [e] Dark conditions. [f] No $[Ru(bpy)_3]Cl_2{\cdot}6H_2O$. [g] No TEOA. [h] Ar instead of CO_2.

As stability and recoverability are vital indicators for evaluating the performance of photocatalysts, $\mathbf{SiW_{12}Co_2}$ was used as an example for detailed evaluation owing to its excellent CO_2RR activity. $\mathbf{SiW_{12}Co_2}$ was immersed in a mixed solvent (MeCN : TEOA = 4 : 1 v/v, 50 mL) as well as aqueous solutions of strong acid (pH = 2) and strong alkali (pH = 13), and no obvious color change of solutions was observed for 24 h (Fig. S20†). According to the PXRD patterns, $\mathbf{SiW_{12}Co_2}$ possesses superb acid–base solvent stability, enabling it to maintain its crystalline integrity throughout the photocatalytic process owing to the stabilized 1D chain structure (Fig. S5, and S18†). Subsequently, photocatalytic cycling tests were conducted to investigate the recyclability of $\mathbf{SiW_{12}Co_2}$ in the CO_2RR. Considering the loss of catalyst during the recycling process, the dosage was enhanced to 2.7 μmol instead of the optimal dosage (0.54 μmol). $\mathbf{SiW_{12}Co_2}$ retains the great bulk of its original activity after four reaction cycles (Fig. 4c), demonstrating that $\mathbf{SiW_{12}Co_2}$ possesses good photocatalytic stability. Besides, the PXRD pattern and IR spectra after the cycling experiments can well match those of prepared samples (Fig. 4f, and S18†), proving that the structure of $\mathbf{SiW_{12}Co_2}$ maintains satisfactory stability in the photocatalytic process.

Mechanism

To fully comprehend the process of photo-excited electron migration, a photoluminescence (PL) quenching experiment was performed and time-resolved fluorescence decay spectra (TRPL) were recorded in the acetonitrile solutions containing photosensitizer (PS) and $\mathbf{SiW_{12}Co_2}$, or electron sacrificial agents, with the solution concentration being proportional to that used for the photocatalytic reaction. As depicted in Fig. 5, the fluorescence intensity of the excited $[Ru(bpy)_3]^{2+}*$ exhibits a gradual decline with augmentation of $\mathbf{SiW_{12}Co_2}$, which is attributed to the attraction of the phosphorescence quenching of excited $[Ru(bpy)_3]^{2+}*$ by continuous electron transfer to $\mathbf{SiW_{12}Co_2}$ (Fig. 5b).[48] In addition, there is almost barely any change in the fluorescence spectra with varying concentrations of TEOA (Fig. 5a). TRPL spectra revealed that the excited luminescence of $[Ru(bpy)_3]^{2+}$ conformed to single-exponential decay kinetics with respect to $\mathbf{SiW_{12}Co_2}$ or TEOA. The lifetimes were designated by values of 384.88 ns and 436.63 ns, which reflect shorter lifespans than that of the separately existing $[Ru(bpy)_3]^{2+}$ (469.41 ns) (Fig. 5d). The shortened lifespan indicates that the luminescence of photosensitizers added to an acetonitrile solution containing $\mathbf{SiW_{12}Co_2}$ could decay more rapidly, validating that the electron transfer from photosensitizers to

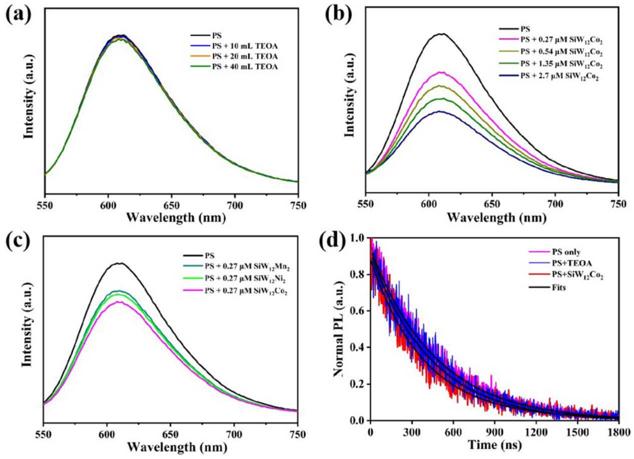

Fig. 5 Emission spectra of $[Ru(bpy)_3]Cl_2$ in different amounts of (a) TEOA ($\lambda_{excitation}$ = 510 nm) and (b) $\mathbf{SiW_{12}Co_2}$. (c) $[Ru(bpy)_3]Cl_2$ in MeCN solutions containing the catalysts $\mathbf{SiW_{12}Co_2}$, $\mathbf{SiW_{12}Ni_2}$ and $\mathbf{SiW_{12}Mn_2}$; (d) time-resolved photoluminescence (TRPL) spectra of $[Ru(bpy)_3]^{2+}$ and TEOA with the addition of $\mathbf{SiW_{12}Co_2}$.

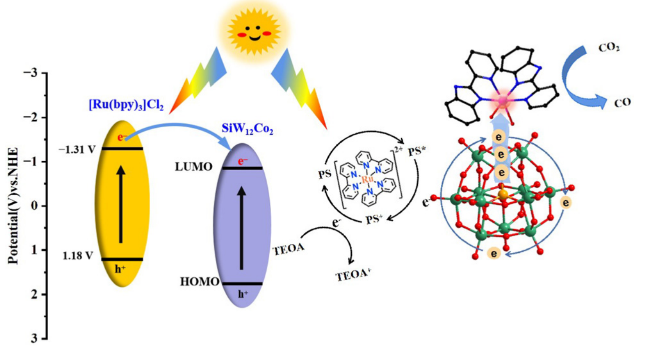

Fig. 6 Schematic diagram of electron transfer energy levels showing the proposed mechanism for photocatalytic CO_2 reduction over $\mathbf{SiW_{12}Co_2}$.

$\mathbf{SiW_{12}Co_2}$ may lead to the phosphorescence quenching of photosensitizers. Compared to TEOA, $\mathbf{SiW_{12}Co_2}$ promotes the separation of electron–hole pairs and suppresses their recombination more efficiently.[49] The results above suggest that the rate of the oxidation process of $\mathbf{SiW_{12}Co_2}$ may be the decisive step of the reaction. Additionally, $[Ru(bpy)_3]^{2+}$ is immediately quenched by $\mathbf{SiW_{12}Co_2}$ rather than TEOA, indicating that the initial step of the photocatalytic CO_2RR primarily involves the transfer of electrons from the excited state of the PS to $\mathbf{SiW_{12}Co_2}$ rather than from the TEOA.[50] Notably, in contrast to $\mathbf{SiW_{12}Ni_2}$ and $\mathbf{SiW_{12}Mn_2}$, the addition of $\mathbf{SiW_{12}Co_2}$ significantly attenuates the PL intensity (Fig. 5c), which proves that the photo-induced electron transfer from $[Ru(bpy)_3]^{2+}$ to $\mathbf{SiW_{12}Co_2}$ is more efficient and effectively inhibits the quick recombination of holes and electrons on $[Ru(bpy)_3]^{2+}$, and their fluorescence quenching ability was in accordance with the aforementioned photocatalytic CO_2RR.[51,52]

The preceding results and discussions have led to the formulation of a possible reaction mechanism and electron transfer pathway for the photocatalytic CO_2 reduction by $\mathbf{SiW_{12}Co_2}$ (Fig. 6). Under visible light irradiation, the photosensitizer $[Ru(bpy)_3]Cl_2$ is motivated to reach its excited state, subsequently undergoing an oxidative quenching process by $\mathbf{SiW_{12}Co_2}$, resulting in the formation of the $[Ru(bpy)_3]^{3+}$ oxidation state. The photogenerated electrons (e^-) in $[Ru(bpy)_3]Cl_2$ leap from the HOMO energy to the LUMO energy level, creating a positively charged hole (h^+) at the HOMO level. The photogenerated electrons spontaneously migrate from $[Ru(bpy)_3]Cl_2$ to the surface of $\mathbf{SiW_{12}Co_2}$ by virtue of the positional matching of the LUMO energy levels between $[Ru(bpy)_3]Cl_2$ and $\mathbf{SiW_{12}Co_2}$.[53] Remarkably, the presence of Co ions in $\mathbf{SiW_{12}Co_2}$ plays a significant role in photocatalytic CO_2 reduction, as they enable the generation of ample numbers of high-energy electrons from the SiW_{12} unit.[14] Ultimately, TEOA serves as a sacrificial electron donor, consuming the photogenerated holes formed in the $[Ru(bpy)_3]^{2+}$ valence band, while the oxidized $[Ru(bpy)_3]^{2+}$ is reduced to the original state $[Ru(bpy)_3]^{3+}$. Simultaneously, TEOA is oxidized to $TEOA^+$, which effectively prevents hole–electron recombination.[54–58]

Conclusions

In general, we have successfully designed and synthesized three isostructural α-Keggin-type POM-based organic–inorganic metal 1D chains ($\mathbf{SiW_{12}Co_2}$, $\mathbf{SiW_{12}Ni_2}$, $\mathbf{SiW_{12}Mn_2}$). Specifically, two adjacent SiW_{12} units are connected *via* dual $[M(pyim)_2]_2^{2+}$ fragments, resulting in the formation of a fairly stable 1D chain with dual nodes. Based on the above UV-vis, Mott–Schottky, and energy band analyses, these three compounds can be used as CO_2RR photocatalysts. Under light irradiation, $\mathbf{SiW_{12}Co_2}$ possesses superior photocatalytic capability to that of both $\mathbf{SiW_{12}Ni_2}$ and $\mathbf{SiW_{12}Mn_2}$. In concrete terms, the optimal dosage of $\mathbf{SiW_{12}Co_2}$ was found to be 0.54 μmol with a formation rate of 10 733 μmol g^{-1} h^{-1}, while the turnover number of CO reached 328 during an eight-hour photocatalysis period. Furthermore, $\mathbf{SiW_{12}Co_2}$ can maintain better activity throughout four reaction cycles. Also, we investigated the electron transfer pathway in the photocatalytic CO_2RR using fluorescence emission spectra and proposed a possible reaction mechanism. The quenching mechanism can help us to better understand the discrepancy in the CO_2RR activities of POM-based compounds modified with different transition metals.

Author contributions

Xin-Lian Chen: writing of the original draft. Jie Wu: review and editing of the manuscript. Ji-Lei Wang: review and editing of the manuscript. Xiao-Mei Liu: review and editing of the manuscript. Hua Mei: writing, review and editing of the manuscript. Yan Xu: formal analysis, writing, review and editing of the manuscript.

Data availability

The authors confirm that the data supporting the findings of this study are available within the article and ESI.†

Conflicts of interest

The authors proclaim no competing financial conflicts.

Acknowledgements

This work was supported by the National Natural Science Foundation of China (92161109), the Postgraduate Research & Practice Innovation Program of Jiangsu Province (SJCX23_0451), and the Cultivation Program for The Excellent Doctoral Dissertation of Nanjing Tech University (2023-10).

References

1 G. V. Last and M. T. Schmick, *Environ. Earth Sci.*, 2015, **74**, 1189–1198.

2 D. C. N. Gruber, B. R. Carter, R. A. Feely, S. Heuven, M. Hoppema, M. Ishii, R. M. Key, A. Kozyr, S. K. Lauvset, C. L. Monaco, J. T. Mathis, A. O. A. Murata, F. F. Perez, C. L. Sabine, T. Tanhua and R. Wanninkhof, *Science*, 2019, **363**, 1193–1199.

3 C. Steinlechner and H. Junge, *Angew. Chem., Int. Ed.*, 2018, **57**, 44–45.

4 X. X. Li, L. Zhang, L. Yuan, T. Wang, L. Z. Dong, K. Huang, J. Liu and Y. Q. Lan, *Chem. Eng. J.*, 2022, **442**, 136157.

5 S. C. Blanco, H. Zhang, J. M. Kim, Y. X. Shen and P. D. Yang, *Nat. Catal.*, 2020, **3**, 245–255.

6 S. R. Nicholson, N. A. Rorrer, A. C. Carpenter and G. T. Beckham, *Joule*, 2021, **5**, 673–686.

7 M. Lu, M. Zhang, J. Liu, T. Y. Yu, J. N. Chang, L. J. Shang, S. L. Li and Y. Q. Lan, *J. Am. Chem. Soc.*, 2022, **144**, 1861–1871.

8 D. Shindell and C. J. Smith, *Nature*, 2019, **573**, 408–411.

9 Y. R. Li, S. T. Li and H. W. Huang, *Chem. Eng. J.*, 2023, **457**, 141179.

10 J. Liang, H. Yu, J. J. Shi, B. Li, L. X. Wu and M. Wang, *Adv. Mater.*, 2023, **35**, 2209814.

11 W. H. Zhang, A. R. Mohamed and W. J. Ong, *Angew. Chem., Int. Ed.*, 2020, **59**, 22894–22915.

12 Y. F. Mu, C. Zhang, M. R. Zhang, W. Zhang, M. Zhang and T. B. Lu, *ACS Appl. Mater. Interfaces*, 2021, **13**, 22314–22322.

13 B. Obama, *Science*, 2017, **355**, 6321.

14 S. H. Guo, X. J. Qi, H. M. Zhou, J. Zhou, X. H. Wang, M. Dong, X. Zhao, C. Y. Sun, X. L. Wang and Z. M. Su, *J. Mater. Chem. A*, 2020, **8**, 11712–11718.

15 X. Y. Xiang, J. L. Zhou, Q. Wang, Y. H. Zhu, Z. T. Zhang, T. C. Ye, J. L. Wang, Q. L. Chen and Y. Xu, *Inorg. Chem.*, 2023, **62**, 5200–5206.

16 C. Wang, C. Y. Zhu, M. Zhang, Y. Geng, Y. G. Li and Z. M. Su, *J. Mater. Chem. A*, 2020, **8**, 14807–14814.

17 J. W. Fu, K. X. Jiang, X. Q. Qiu, J. G. Yu and M. Liu, *Mater. Today*, 2020, **32**, 222–243.

18 Y. J. Gao, L. Zhang, Y. M. Gu, W. W. Zhang, Y. Pan, W. H. Fang, J. Ma, Y. Q. Lan and J. Bai, *Chem. Sci.*, 2020, **11**, 10143–10148.

19 Y. Bai, P. Yang, L. Wang, B. Yang, H. Q. Xie, Y. Zhou and L. Q. Ye, *Chem. Eng. J.*, 2019, **360**, 473–482.

20 Y. Z. Zhu, C. Gao, S. Bai, S. M. Chen, R. Long, L. Song, Z. Q. Li and Y. J. Xiong, *Nano Res.*, 2017, **10**, 3396–3406.

21 X. X. Li, J. Liu, L. Zhang, L. Z. Dong, Z. F. Xin, S. L. Li, X. Q. Huang Fu, K. Huang and Y. Q. Lan, *ACS Appl. Mater. Interfaces*, 2019, **11**, 25790–25795.

22 Z. Zeb, Y. C. Huang, L. L. Chen, W. B. Zhou, M. B. Liao, Y. Y. Jiang, H. T. Li, L. M. Wang, L. Wang, H. Wang, T. Wei, D. J. Zang, Z. J. Fan and Y. G. Wei, *Coord. Chem. Rev.*, 2023, **482**, 215058.

23 Y. J. Wang, Z. F. Qiu, Y. Zhang, F. F. Wang, Y. Zhao and W. Y. Sun, *Dalton Trans.*, 2024, **53**, 3685–3689.

24 A. V. Anyushin, A. Kondinski and T. N. Parac-Vogt, *Chem. Soc. Rev.*, 2020, **49**, 382–432.

25 S. S. Wang and G. Y. Yang, *Chem. Rev.*, 2015, **115**, 4893–4962.

26 L. X. Cai, S. C. Li, D. N. Yan, L. P. Zhou, F. Guo and Q. F. Sun, *J. Am. Chem. Soc.*, 2018, **140**, 4869–4876.

27 M. Samaniyan, M. Mirzaei, R. Khajavian, H. Eshtiagh-Hosseini and C. Streb, *ACS Catal.*, 2019, **9**, 10174–10191.

28 J. L. Wang, J. P. Cao, Z. Y. Du, X. M. Liu, J. N. Li, Q. D. Ping, T. T. Zang and Y. Xu, *Chin. Chem. Lett.*, 2023, **34**, 106917.

29 Y. H. Zhu, J. B. Yang, P. F. Yan, Z. M. Dong, H. Mei and Y. Xu, *J. Mater. Chem. A*, 2024, **12**, 5340–5347.

30 L. Yang, Z. Zhang, C. N. Zhang and X. L. Wang, *Rare Met.*, 2024, **43**, 236–246.

31 J. L. Wang, X. M. Liu, Z. Y. Du and Y. Xu, *Dalton Trans.*, 2021, **50**, 7871–7886.

32 N. Li, J. Liu, J. J. Liu, L. Z. Dong, Z. F. Xin, Y. L. Teng and Y. Q. Lan, *Angew. Chem., Int. Ed.*, 2019, **58**, 5226–5231.

33 N. Li, J. Liu, B. X. Dong and Y. Q. Lan, *Angew. Chem., Int. Ed.*, 2020, **59**, 20779–20793.

34 T. J. Wilke and M. A. Barteau, *J. Catal.*, 2020, **382**, 286–294.

35 P. F. Yan, X. Y. Li, J. L. Wang, J. H. Pan, H. Xu, Y. H. Zhu, Q. L. Chen, H. Mei and Y. Xu, *Mol. Catal.*, 2024, **561**, 114162.

36 Y. H. Zhu, P. F. Yan, L. T. Xu, Z. Y. Du, H. Mei and Y. Xu, *Dalton Trans.*, 2024, **53**, 7257–7262.

37 C. L. Wu, X. H. Qiao, C. M. Robertson, S. J. Higgins, C. Cai and R. N. u. A. Vezzoli, *Angew. Chem., Int. Ed.*, 2020, **59**, 12029–12034.

38 L. Z. Qiao, M. Song, A. F. Geng and S. Yao, *Chin. Chem. Lett.*, 2019, **30**, 1273–1276.

39 Y. Y. Li, A. G. Walsh, D. S. Li, D. Do, H. Ma, C. H. Wang, P. Zhang and X. T. Zhang, *Nanoscale*, 2020, **12**, 17245–17252.

40 K. Talbi, F. Penas-Hidalgo, A. L. Robinson, P. Gotico, W. Leibl, P. Mialane, M. Gomez-Mingot, M. Fontecave,

A. Solé-Daura, C. Mellot-Draznieks and A. Dolbecq, *Appl. Catal., B*, 2024, **345**, 123681.

41 X. X. Li, L. Zhang, J. Liu, L. Yuan, T. Wang, J. Y. Wang, L. Z. Dong, K. Huang and Y. Q. Lan, *J. Am. Chem. Soc. Au*, 2021, **1**, 1288–1295.

42 M. Cheng, Z. Zhang, H. L. Li and G. Y. Yang, *Inorg. Chem. Commun.*, 2018, **96**, 69–72.

43 F. Y. Cui, X. Y. Ma, C. Li, T. Dong, Y. Z. Gao, Z. G. Han, Y. N. Chi and C. W. Hu, *J. Solid State Chem.*, 2010, **183**, 2925–2931.

44 D. D. Zhu, J. L. Liu and S. Z. Qiao, *Adv. Mater.*, 2016, **28**, 3423–3452.

45 J. D. Hong, W. Zhang, J. Ren and R. Xu, *Anal. Methods*, 2013, **5**, 1073–1356.

46 Y. X. Pan, Y. You, S. Xin, Y. Li, G. Fu, Z. Cui, Y. L. Men, F. F. Cao, S. H. Yu and J. B. Goodenough, *J. Am. Chem. Soc.*, 2017, **139**, 4123–4129.

47 J. Du, Y. Y. Ma, X. Xin, H. Na, Y. N. Zhao, H. Q. Tan, Z. G. Han, Y. G. Li and Z. H. Kang, *Chem. Eng. J.*, 2020, **398**, 125518.

48 J. N. Qin, S. B. Wang and X. C. Wang, *Appl. Catal., B*, 2017, **209**, 476–482.

49 T. Maschmeyer and M. Che, *Angew. Chem., Int. Ed.*, 2010, **49**, 1536–1539.

50 M. Wang, J. X. Liu, C. M. Guo, X. S. Gao, C. H. Gong, Y. Wang, B. Liu, X. X. Li, G. G. Gurzadyan and L. C. Sun, *J. Mater. Chem. A*, 2018, **6**, 4768–4775.

51 W. T. Eckenhoff, *Coord. Chem. Rev.*, 2018, **373**, 295–316.

52 V. S. Thoi, N. Kornienko, C. G. Margarit, P. D. Yang and C. J. Chang, *J. Am. Chem. Soc.*, 2013, **135**, 14413–14424.

53 C. Gao, S. M. Chen, Y. Wang, J. W. Wang, X. S. Zheng, J. F. Zhu, L. Song, W. K. Zhang and Y. J. Xiong, *Adv. Mater.*, 2018, **30**, 1704624.

54 C. M. Gao, H. N. Yu, L. N. Zhang, Y. H. Zhao, J. X. Xie, C. J. Li, K. Cui and J. H. Yu, *Anal. Chem.*, 2020, **92**, 2902–2906.

55 S. L. Xie, J. Liu, L. Z. Dong, S. L. Li, Y. Q. Lan and Z. M. Su, *Chem. Sci.*, 2019, **10**, 185–190.

56 K. Zhao, S. L. Zhao, C. Gao, J. Qi, H. J. Yin, D. Wei, M. F. Mideksa, X. L. Wang, Y. Gao, Z. Y. Tang and R. B. Yu, *Small*, 2018, **14**, 1800762.

57 S. Linic, P. Christopher and D. B. Ingram, *Nat. Mater.*, 2011, **10**, 911–921.

58 J. L. Wang, H. Xu, Q. Wang, J. L. Zhou, X. Y. Xiang, S. M. Li, H. Mei and Y. Xu, *Chem. Eng. J.*, 2023, **474**, 145662.